

# Calibration of a multi-mobile coil magnetic manipulation system utilizing a control-oriented magnetic model

Nahashon O. Osinde<sup>a,b</sup>, Maxime Etiévant<sup>a</sup>, Jean Bosco Byiringiro<sup>b</sup>, Nicolas Andreff<sup>a,\*</sup>

<sup>a</sup>*FEMTO-ST Institute, Université Bourgogne Franche-Comté, 15B Avenue des Montboucons, Besançon, 25000, France*

<sup>b</sup>*Mechatronic Engineering, Dedan Kimathi University of Technology, Nyeri, Kenya*

## Abstract

In this paper, we address the calibration of a family of magnetic manipulation systems composed of several coils that are moved around by serial robot manipulators. We show in this paper that the calibration of the whole system ultimately results in calibrating the manipulator and coil separately up to an unknown rigid transformation. For calibration of the coil, we propose to use a model that has not been used so far in the literature; a control-oriented model which is sufficiently accurate and computes the magnetic field in real time. A protocol for calibrating the magnetic manipulation system using the Nelder-Mead algorithm to estimate the model parameters is presented. Calibration was performed through simulations and validated experimentally on a physical system. It was observed that the root mean square error was reduced by 37% after calibration of the physical system, indicating an improvement in accurately estimating the magnetic model.

**Keywords:** calibration, multi-mobile coil, magnetic manipulation, microrobotics, numerical algorithm

## 1. Introduction

In the last decade, there has been noteworthy development in the field of microrobotics, largely attributed to the advancements of micro-fabrication techniques and microscopy [1]. Researchers are exploring various ways and techniques in which systems can be developed to perform microscale tasks. Micro-robots have several applications in engineering as well as in the medical field. These include micro-manipulation, micro-assembly, performing minimally invasive surgical operations and performing targeted diagnosis and drug delivery [2, 3, 4]. Applications such as minimally invasive surgery have several benefits which include; reduction in recovery time, medical complication and infection risks [5].

With the size of microrobots, there is difficulty in controlling them due to viscous forces dominating inertia forces at the micro-scale. Therefore, building of robots in the microscale has technical limitations to engineers since scaling down of concepts and designs used in the macro-scale is difficult and at times impractical. Engineers therefore have to abandon intuition gained from designing in the macro-world and instead rely on the physics governing microrobot design and analysis. Descending in scale, it becomes more and more interesting to eliminate energy storage elements and introduce remote actuation rather than design a sophisticated microrobot. An efficient way to control microrobots wirelessly is by use of magnetic fields. In addition, magnetic fields are easy to produce, have

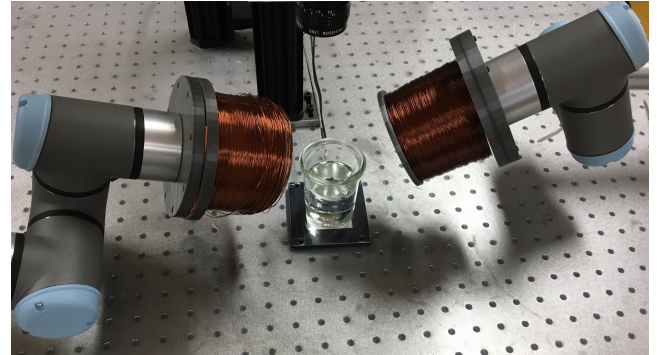


Figure 1: Magnetic manipulation of a microrobot using two coils. Each coil is being displaced by a UR3 (Universal Robot) serial robot.

limited interaction with the human body and are able to transfer large amounts of power [6].

Electromagnetic coils are a suitable choice in generating magnetic fields since they are inactive when powered down [7]. By modulating the magnetic field, it is possible to generate a force and torque which can be used in the control of a microrobot. In particular, higher dexterity and efficiency can be achieved by modulating the magnetic field through both current variation and motion of the coils as initially shown in [8] and later exploited in [9, 10, 11]. The use of mobile coils present several advantages over the use of stationary bigger coils when a large footprint of the patient workspace is needed. Large coils which are heavy may result in complexities in the structural design thereby making the manufacturing process more expensive [12]. In addition, larger coils would have higher inductance which would limit the control frequency, increase the power

\*Corresponding author: nicolas.andreff@femto-st.fr

<sup>1</sup>Emails:nahashon.osinde@femto-st.fr(N.O.Osinde), maxime.etievant@femto-st.fr(M.Etiévant),jean.bosco@dkut.ac.ke(J. Byiringiro),nicolas.andreff@femto-st.fr (N. Andreff)

consumption and the heat dissipated. Therefore, in a bid to have a large workspace with minimal energy expenditure, it is essential to use mobile coils and move them close to the area of manipulation.

Consider a magnetic manipulation system having several coils made by mobile serial robots as seen in Figure 1. For highly accurate positioning and control of a microrobot through magnetic manipulation, a control-oriented model that is fast and accurate to compute the magnetic field is required [13]. Accurate modeling of the magnetic field can be achieved using Finite Element Models but this is too slow for control. For control, one usually relies either on the simplified dipole model or on prerecorded magnetic field. It has been shown in [14] that the dipole model is accurate for distances far away from the magnet. These approaches are not perfectly suited to multi-mobile electromagnetic manipulation. To perform multi-mobile electromagnetic manipulation closed-loop control, a control-oriented model is needed, i.e. a model that provides a trade-off between the computation time and accuracy. One such model based on complete elliptic integrals has been shown in [15] to be suitable for closed-loop control of magnetically actuated robots. A cost effective way to improve this model further is through model-based calibration [16, 17]. Calibration is a process through which parameters to a given system model are identified and adjusted such that the output of the model fits well to the actual output of the system [18]. Through calibration of an electromagnetic system, the positioning accuracy of a microrobot can thus be enhanced by adjusting model parameters rather than altering the mechanical structure of the electromagnetic system. In [19] a generic magnetic model based on a multi-source spherical multipole expansion was calibrated using nonlinear least squares. Although numerically efficient, the model used in [19] was less grounded into physics as the model in [15] and was also not assessed in close vicinity of the coils.

In this paper a model of the full multi-mobile magnetic manipulation system (including kinematics of the manipulator) is presented. It is shown that the calibration of the system needs to be split into several subsystems which eventually results in calibrating the coil and a reference rigid transformation only. The coil was modelled using the control-oriented model which provides a trade-off between its accuracy and computation speed [15]. Sensitivity analysis on the model to investigate the significance of the model parameters is also presented.

This paper is composed of six sections. We first present the background on calibration in Section 2. Modelling of the magnetic manipulation system is highlighted in Section 3. Section 4 presents calibration of the mobile magnetic manipulation system and Section 5 is devoted to the calibration results. Conclusions and perspectives are drawn in Section 6.

## 2. Calibration background

Calibration has several phases which include; modelling, measurement, parameter identification, error compensation and finally validation [20]. The steps of calibration are described briefly in the subsequent sub-topics with specific insight on magnetic manipulation.

### 2.1. Modelling

The first step of calibration in this context is the formulation of a mathematical model that describes the magnetic field. Several models are in use for the computation of the magnetic field [11]. Nonetheless, for real time control a model that is both accurate and fast to compute is needed. It has been shown in [15] that the magnetic model based on complete elliptic integrals is accurate in the whole workspace area and takes less time to compute as compared to existing magnetic models. Moreover, when the coils are mobile, a kinematic model of the moving structure is needed.

### 2.2. Measurement

This step involves collection of magnetic field measurement data that will be used in the calibration process. This data is obtained by measuring the magnetic field generated by the coil in the workspace using a Hall effect sensor.

### 2.3. Parameter identification

Parameter identification can be defined as the numerical procedure used to determine parameter values to the magnetic model. This step has been addressed by several researchers and various parameter identification algorithms have been used. In this paper, we rely on the output error identification method [20, 21] as shown in Figure 2.

Let  $\xi$  define the set of parameters in the model, the aim is to minimize the objective function generally defined from the root mean square error (RMSE). The RMSE highlights the discrepancy between the magnetic field computed from the model and the one obtained from the measurement. To compute the deviation,  $\epsilon_i$ , at a particular measurement configuration,  $i$ , in the workspace, equation (1) is used:

$$\epsilon_i(\xi) = \hat{\mathbf{B}}_i(I, {}^w T_c, \xi) - \mathbf{B}_i(I, {}^w T_c) \quad (1)$$

where  $\hat{\mathbf{B}}_i$  is the estimated magnetic field from the model using the control inputs ( $I$  the current in the coil,  ${}^w T_c$  the pose of the coil in space) and the model parameters,  $\xi$ .  $\mathbf{B}_i$  is the measured output.

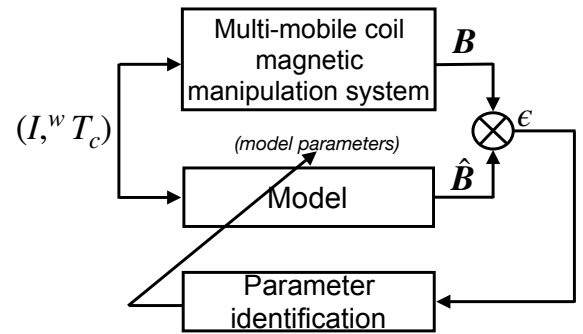


Figure 2: Calibration process through output error minimisation.

RMSE from several  $m$  points in the workspace is therefore computed using equation (2):

$$RMSE = \frac{1}{2} \sqrt{\frac{1}{m} \sum_{i=1}^m \|\epsilon_i\|^2} \quad (2)$$

The resulting cost function that needs to be minimized using a numerical algorithm so as to obtain the optimal parameter values  $\xi^*$  is:

$$\xi^* = \underset{\{\xi\}}{\operatorname{argmin}} \frac{1}{2} \sqrt{\frac{1}{m} \sum_{i=1}^m \|\boldsymbol{\epsilon}_i\|^2} \quad (3)$$

Algorithms used in parameter identification include Sequential Quadratic Programming (SQP), Nelder-Mead, Levenberg-Marquardt, genetic algorithm among many others [22].

#### 2.4. Error compensation

Error compensation (also referred to as the correction step) involves adjusting the parameter values in the control-oriented model with the values obtained after parameter identification. This is demonstrated by the arrow crossing the 'Model' box in Figure 2.

#### 2.5. Validation

This is the final step in the calibration process. It involves comparison of the magnetic field obtained from the modified model and the measured one. Measurement data used in this step must be statistically independent from the data used in parameter identification. The error computed from equation (2) should be as minimum as possible, so as to ascertain that the model is valid. If the model is not validated, parameter identification is done again, or new measurement data are taken or a new model of the electromagnetic system is formulated again.

### 3. Modelling of the magnetic manipulation system

#### 3.1. Generic case

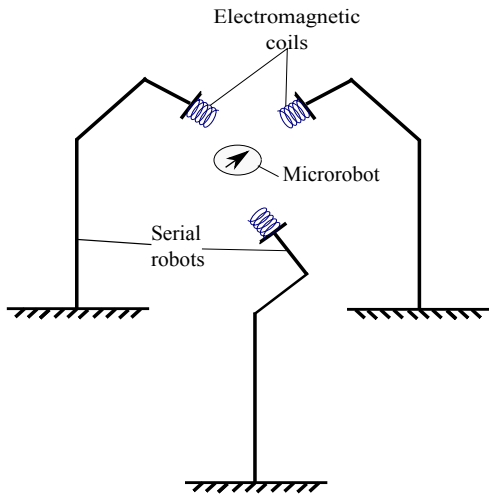


Figure 3: Schematic of a magnetic manipulation system.

A generic case study will be first developed. A schematic of a magnetic manipulation system is as shown in Figure 3. It consists of several serial robots, each with a magnetic coil attached to the end-effector. Further developing this generic case study, each coil generates a magnetic field  $\mathbf{B}_j$ . The total field at a position configuration  $P$  in the world reference

frame for  $n$  coils, assuming the superposition theorem holds is  ${}^w\mathbf{B}({}^wP) = \sum_{j=1}^n {}^w\mathbf{B}_j({}^wP)$  [3]. To obtain  $\mathbf{B}_j$ , modelling of one circular coil loop, the coil and the robotic manipulator needs to be done.

#### 3.2. Modelling of one circular coil loop

Consider a circular current loop of one coil in the spherical coordinate system with loop radius  $a$  centered at  $O$  as shown in Figure 4.

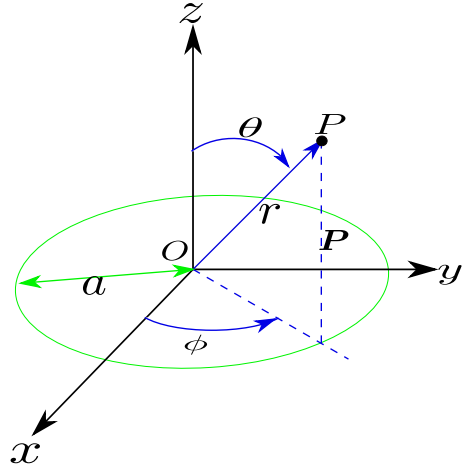


Figure 4: Circular current coil loop.

The magnetic field in a point  $P$  of spherical coordinates  $(r, \theta, \phi)$  computed using complete elliptic integrals is [15]:

$$\begin{cases} B_r(r, \theta) &= \frac{\mu_0 I}{\pi} \frac{a^2}{\sqrt{a^2+r^2+2arsin(\theta)}} \frac{E(k)cos(\theta)}{a^2+r^2-2arsin(\theta)} \\ B_\theta(r, \theta) &= \frac{\mu_0 I}{\pi} \frac{1}{\sqrt{a^2+r^2+2arsin(\theta)}} f(r, \theta) \\ B_\phi &= 0 \\ f(r, \theta) &= \left[ \frac{E(k)(r^2+a^2\cos(2\theta))}{2\sin(\theta)(a^2+r^2-2arsin(\theta))} - \frac{K(k)}{2\sin(\theta)} \right] \end{cases} \quad (4)$$

where  $\mu_0$  is the vacuum permittivity,  $K(k)$  and  $E(k)$  are the complete elliptic integral functions of first and second kind:

$$\begin{aligned} K(k) &= \int_0^{\frac{\pi}{2}} \frac{1}{\sqrt{1-k^2\sin^2\theta}} d\theta \\ E(k) &= \int_0^{\frac{\pi}{2}} \sqrt{1-k^2\sin^2\theta} d\theta \end{aligned} \quad (5)$$

and  $k$  is the modulus of the elliptic integral functions:

$$k^2 = \frac{4arsin\theta}{a^2 + r^2 + 2arsin\theta} \quad (6)$$

However, the expressions in equation (4) are not defined for  $k = 0$ . When  $k \ll 1$ , the continuity is done by using [23]:

$$\begin{aligned} K(k) &= \frac{\pi}{2} + k^2 \frac{\pi}{8} + k^4 \frac{9\pi}{128} + O(k^4) \\ E(k) &= \frac{\pi}{2} - k^2 \frac{\pi}{8} - k^4 \frac{3\pi}{128} + O(k^4) \end{aligned} \quad (7)$$

With the continuity expression in equation (7), equation (4) is simplified and the magnetic field for  $k \ll 1$  becomes:

$$\begin{cases} B_r(r, \theta) = \frac{\mu_0 I a^2}{4} \cos(\theta) \frac{(2a^2 + \sin(\theta)ar + 2r^2)}{(a^2 + 2\sin(\theta)ar + r^2)^{\frac{5}{2}}} \\ B_\theta(r, \theta) = -\frac{\mu_0 I a^2}{4} \sin(\theta) \frac{(2a^2 + \sin(\theta)ar + r^2)}{(a^2 + 2\sin(\theta)ar + r^2)^{\frac{5}{2}}} \\ B_\phi = 0 \end{cases} \quad (8)$$

In addition, note for consistency sake that when  $r \gg a$ , the expression in equation (8) is simplified into the dipole approximation [24].

### 3.3. Modelling of one coil

The magnetic coil is composed of many single loops. Figure 5 shows the actual coil and its schematic used in this case study. Although the actual wiring is not perfectly known or made, we assume a regular model as shown in Figure 6, where  $d$  is the diameter of the copper wire used in the winding. Copper wire is wound cylindrically as seen in Figure 5a. Loops of wire wound in the radial direction are referred to as radial loops and loops of wire along the axis are referred to as axial loops. They are shown in the schematic of the coil in Figure 5b.

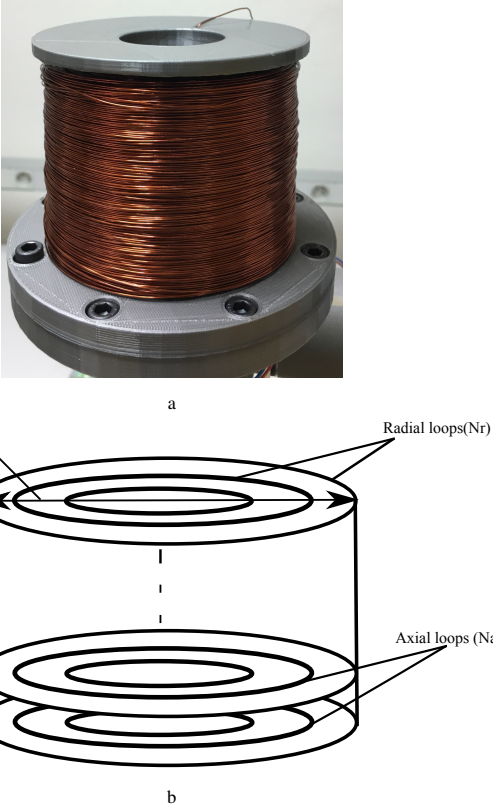


Figure 5: (5a) Side view of the actual coil. (5b) Schematic representation of the various parameters that need to be identified during the calibration phase.

For modelling and later calibration to be done on the coil, information from the model given in equation (4) needs to be extracted [25]. These comprises of: constants, measured variables and parameters to be estimated. From the model, the constant is vacuum permittivity,  $\mu$ , measured variables are the po-

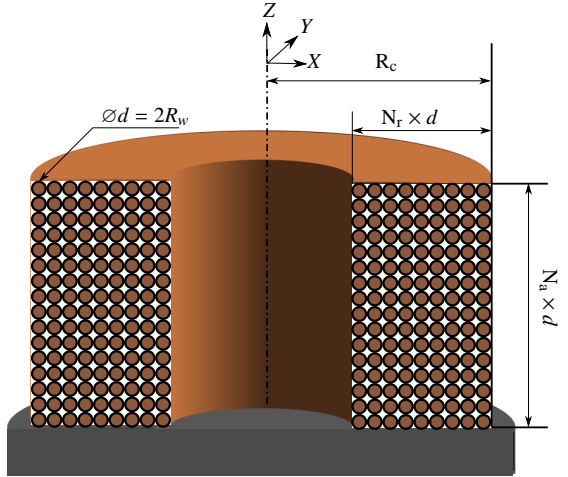


Figure 6: Side view of a regular model of the coil.

sition of the measurement point (obtained from  $r$  and  $\theta$ ) and the parameters to be estimated are:

- External loop radius ( $R_c$ ).
- Wire radius ( $R_w$ ).
- Number of loops radially ( $N_r$ ).
- Number of loops axially ( $N_a$ ).

These parameters need to be taken into account in equation (4) so as to compute the total magnetic field in the coil. The parameter values to the assumed regular model of the coil might not be correct, hence the need for calibration to identify them.

Expressing the radius,  $a$  and height,  $dz$  of each loop as a function of its index in the radial wiring,  $n_r$  and axial wiring,  $n_a$ :

$$a(n_r) = (R_c - R_w) - (2R_w(n_r - 1)) \quad (9)$$

$$dz(n_a) = (2R_w(n_a - 1)) + R_w \quad (10)$$

There is also need to compute  $r$  and  $\theta$  for each loop in the coil:

$$r(P, n_a) = (X^2 + Y^2 + (Z + dz(n_a))^2)^{\frac{1}{2}} \quad (11)$$

$$\theta(P, n_a) = \arccos\left(\frac{Z + dz(n_a)}{r(P, n_a)}\right) \quad (12)$$

where  $P = (X, Y, Z)^T$  are the coordinates of the point  $P$  in the reference frame  $\mathcal{F}_c$  attached to the coil.

The magnetic field sum for each loop axially and radially in the coil reference frame is then considered to compute the total magnetic field:

$$\begin{cases} {}^c B_r(P) = \sum_{n_a=1}^{N_a} \sum_{n_r=1}^{N_r} B_r(r(P, n_a), \theta(P, n_a), a(n_r)) \\ {}^c B_\theta(P) = \sum_{n_a=1}^{N_a} \sum_{n_r=1}^{N_r} B_\theta(r(P, n_a), \theta(P, n_a), a(n_r)) \\ {}^c B_\phi(P) = 0 \end{cases} \quad (13)$$

### 3.4. Modelling of the full multi-mobile magnetic manipulation system

The multi-mobile electromagnetic manipulation system is first subdivided into several arms. Figure 7 shows the schematic representation of one arm in two configurations.  $\mathcal{F}_w$  is the

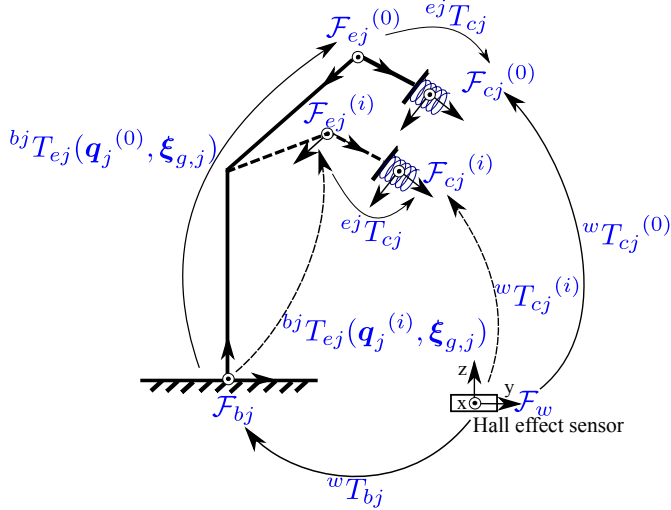


Figure 7: Schematic of one arm of the magnetic manipulation system in a reference (0) configuration and in a generic (i) one.

world coordinate system attached to the static Hall effect sensor used for calibration,  $\mathcal{F}_{bj}$  the  $j$ 'th robot base frame,  $\mathcal{F}_{ej}$  the  $j$ 'th robot end-effector frame and  $\mathcal{F}_{cj}$  is the  $j$ 'th robot coil frame. Expressing the magnetic field in the world frame at the origin of  $\mathcal{F}_w$  (measurement point):

$${}^w\tilde{\mathbf{B}}_j({}^w\tilde{O}) = {}^wT_{cj} {}^c\tilde{\mathbf{B}}_j(\boldsymbol{\xi}_{m,j}, {}^wT_{cj}^{-1} {}^w\tilde{O}) \quad (14)$$

where  $\tilde{\mathbf{B}} = \begin{pmatrix} \mathbf{B} \\ 0 \end{pmatrix}$ ,  ${}^w\tilde{O} = \begin{pmatrix} {}^wO \\ 1 \end{pmatrix}$  are the projective coordinates of vector  $\mathbf{B}$  and point  $O$ ,  $\boldsymbol{\xi}_{m,j}$  is the vector of coil model parameters and  ${}^wT_{cj} = \begin{pmatrix} {}^wR_{cj} & {}^w\mathbf{t}_{cj} \\ 0 & 1 \end{pmatrix}$  which is the pose of the coil frame relative to the world frame given by the kinematic chain:

$${}^wT_{cj} = {}^wT_{bj} FKM(\mathbf{q}_j, \boldsymbol{\xi}_{g,j}) {}^{ej}T_{cj} \quad (15)$$

where *FKM* is the forward kinematic model of the robot,  $\mathbf{q}_j$ , the variable robot joint values and  $\boldsymbol{\xi}_{g,j}$ , the constant kinematic parameters to the robot.  ${}^wT_{bj}$  and  ${}^{ej}T_{cj}$  are also constant transformations.

The total magnetic field at the origin of the Hall effect sensor in the world frame from all the arms of the multi-mobile electromagnetic system is therefore given by:

$$\begin{aligned} {}^w\tilde{\mathbf{B}}({}^wT_{bj}, \mathbf{q}_j, \boldsymbol{\xi}_{g,j}, {}^{ej}T_{cj}, \boldsymbol{\xi}_{m,j}, {}^w\tilde{O}) = \\ \sum_{j=1}^n {}^wT_{cj}(\cdot) {}^c\tilde{\mathbf{B}}_j(\boldsymbol{\xi}_{m,j}, {}^wT_{cj}(\cdot)^{-1} {}^w\tilde{O}) \end{aligned} \quad (16)$$

where  ${}^wT_{cj}(\cdot)$  means that equation (15) is used to compute  ${}^wT_{cj}$  using the variable  $\mathbf{q}_j$  and constant parameters  ${}^wT_{bj}$ ,  ${}^{ej}T_{cj}$  and  $\boldsymbol{\xi}_{g,j}$ .

## 4. Calibration of the mobile magnetic manipulation system

Using equation (16) directly in the calibration cost function would yield a high dimensional numerical problem. Careful examination of the equation shows that the numerical problem can be simplified.

### 4.1. Simplifying the calibration problem

#### 4.1.1. Separate calibration of each arm

In building the model, we assumed as most researchers [3] that the inter-coil magnetic interferences are neglectable and that the superposition theorem holds. Additionally, since the coils can be individually turned on and off, a reasonable calibration protocol is to turn them on one at a time. As a consequence, only one term in equation (16) will be non-zero at a time and each arm can thus be simplified in  $n$  subcalibration problems for each  $m$  configuration.

$$\forall j = 1..n \underset{{}^wT_{bj}, {}^{ej}T_{cj}, \boldsymbol{\xi}_{g,j}, \boldsymbol{\xi}_{m,j}}{\operatorname{argmin}} \frac{1}{2} \sqrt{\frac{1}{m} \sum_{i=1}^m \| {}^w\hat{\mathbf{B}}_j^{(i)} - {}^wT_{cj}(\cdot)^{(i)} {}^c\mathbf{B}_j^{(i)}(\cdot) \|^2} \quad (17)$$

#### 4.1.2. Robot forward kinematic calibration

To use the *FKM*, the robot needs to be calibrated. Calibration of the serial robot necessitates moving it in its whole workspace and taking measurements. Using directly equation (16), a full calibration of both kinematic and magnetic parts of the model is not possible. Indeed, the coils mounted on the end-effector generate a magnetic field in a limited workspace (near the coil). Measurements of the magnetic field in the serial robot workspace which is significantly larger than the coil workspace would be zero at most locations. To get relevant data on the magnetic field, we are therefore restricted to a small workspace i.e. near the coil. On that account, the calibration of the kinematic model of the robot needs to be done separately.

#### 4.1.3. Robot-world and hand-coil calibration

With the assumption that the robot is already calibrated, what remains of importance is the calibration of the coil as well as the robot base to world ( ${}^wT_{bj}$ ) and hand-coil ( ${}^{ej}T_{cj}$ ) transformations. Determining these two transformations is a problem similar to the simultaneous robot-world and hand-eye calibration problem in [26]. However, since we cannot compute or measure the full  $4 \times 4$  transformation  ${}^wT_{cj}$  but only the  $3 \times 1$  magnetic field value at the sensor point  $\mathbf{B}({}^wT_{cj})$ , we need to adapt the calibration method to this partial information through further simplification.

#### 4.1.4. Simplified calibration problem

Taking into account all the considerations above, the remaining unknown parameters are the transformation  ${}^wT_{cj}$  of the  $j$ 'th robot coil with respect to the sensor and  $\boldsymbol{\xi}_{m,j}$  the magnetic parameters to the  $j$ 'th coil model. Keeping the idea of hand-eye calibration [27], a 'relative' model using relative displacement of the coil with respect to a reference configuration instead of an 'absolute' model is written. Consider configuration (0) and

(i) after motion of the robot arm in Figure 7, the relative model is given by expressing  ${}^wT_{cj}^{(i)}(\cdot)$  as:

$${}^wT_{cj}^{(i)}(\cdot) = {}^wT_{cj}^{(0)} {}^{ej}T_{cj}^{-1} {}^{bj}T_{ej}({q}_j^{(0)}, \xi_{g,j})^{-1} {}^{bj}T_{ej}({q}_j^{(i)}, \xi_{g,j}) {}^{ej}T_{cj} \quad (18)$$

Thus,

$${}^wT_{cj}^{(i)}(\cdot) = {}^wT_{cj}^{(0)} {}^{ej}T_{cj}^{-1} {}^{(0)}\Delta T_{(i)} {}^{ej}T_{cj} \quad (19)$$

where  ${}^{(0)}\Delta T_{(i)}$  is the displacement of the end-effector from  $\mathcal{F}_{ej}^{(0)}$  to  $\mathcal{F}_{ej}^{(i)}$ . For the experimental protocol, we propose to use only pure translations such that  $\Delta R = I$ , therefore,  ${}^{(0)}\Delta T_{(i)} = \begin{pmatrix} {}^{(0)}\Delta t_{(i)} \\ 0 & 1 \end{pmatrix}$ . Indeed, it makes it simpler for the user and reduces again the complexity of the calibration. Under this protocol, equation (19) develops as:

$${}^wT_{cj}^{diff}(\cdot) = {}^wT_{cj}^{(0)} \begin{pmatrix} I & {}^{ej}\mathbf{R}_{cj}^T {}^{(0)}\Delta t_{(i)} \\ 0 & 1 \end{pmatrix} \quad (20)$$

and thus:

$$\begin{aligned} {}^wT_{cj}^{diff}(\cdot)^{-1} &= \begin{pmatrix} I & -{}^{ej}\mathbf{R}_{cj}^T \Delta t \\ 0 & 1 \end{pmatrix} {}^wT_{cj}^{(0)-1} \\ &= \begin{pmatrix} {}^w\mathbf{R}_{cj}^{T(0)} & -{}^{ej}\mathbf{R}_{cj}^T {}^{(0)}\Delta t_{(i)} - {}^w\mathbf{R}_{cj}^{T(1)} {}^w\mathbf{t}_{cj}^{(0)} \\ 0 & 1 \end{pmatrix} \end{aligned} \quad (21)$$

Since we have the computer aided design (CAD) values of the mounting brackets of the coil to the end-effector, we can reasonably estimate the hand-coil transformation up to an accuracy which is in the order of magnitude of the *FKM* accuracy. Depending on the machine used in the fabrication of the mounting brackets, the hand-coil transformation accuracy can even be better.

The error on  ${}^{ej}\mathbf{R}_{cj}^T {}^{(0)}\Delta t_{(i)}$  is therefore of the same order of magnitude as the error on  $\Delta t$ . It can be noticed that  ${}^{ej}\mathbf{t}_{cj}$  vanishes and only  ${}^{ej}\mathbf{R}_{cj}$  is needed. We can then use the CAD values for  ${}^{ej}\mathbf{R}_{cj}^T$ . Moreover, in most set-ups,  ${}^{ej}\mathbf{R}_{cj}$  will be a  $\frac{\pi}{2}$  rotation or the identity. Consequently, removing the projective notation the calibration becomes:

$$\underset{\{{}^wT_{cj}^{(0)}, \xi_m\}}{\text{argmin}} \frac{1}{2} \sqrt{\frac{1}{m} \sum_{i=1}^m \| {}^w\hat{\mathbf{B}}^{(i)} - {}^w\mathbf{R}_{cj}^{(0)cj} {}^c\mathbf{B}_j^{(i)}(\xi_{m,j},} \quad (22)$$

$$(-{}^{ej}\mathbf{R}_{cj}^T {}^{(0)}\Delta t_{(i)} - {}^w\mathbf{R}_{cj}^{(0)T} {}^w\mathbf{t}_{cj}^{(0)}) \| \|^2$$

where  ${}^w\hat{\mathbf{B}}^{(i)}$  is the measured magnetic field at configuration (i) of the robot using the Hall effect sensor and  ${}^c\mathbf{B}_j^{(i)}$  is the estimated magnetic field at configuration (i) using the model. The values to  ${}^wT_{cj}^{(0)}$  and  $\xi_m$  are estimated through calibration.

#### 4.2. Sensitivity analysis of the coil parameters

The coil model has many parameters and not all of them may have a major influence on the output variability. In a bid to understand the significance of each parameter, a sensitivity analysis was conducted. This is a fundamental step before calibration [28]. The elemental approach to performing sensitivity

analysis is utilizing partial differentiation and the simplest one, varying one factor at a time (OAT). Depending on the nature of the model, partial differentiation may become so complex rendering implementation impractical. OAT is referred to as 'local sensitivity' since the analysis is only done for the selected point estimates and not the entire distribution space. Another approach to sensitivity analysis is through factorial designs. Using factorial designs for sensitivity analysis involves choosing a parameter distribution space and implementing the model for all combinations in the distribution space. However, as the number of parameters and size of the distribution space increases, so does the number of runs. Nevertheless, the same information can be obtained through fractional factorial design approaches such as Box-Behnken and Taguchi [29]. For this research, factorial design was used, it has the following advantages:

- Parameter interaction effects are able to be analysed and assessed. This leads to good understanding of how the output response changes with the input parameters.
- Output response analysis is able to be done at different parameter levels yielding valid conclusions over a wide range of experimental conditions.

A full factorial design with seven levels of unitary step for the parameter distribution space as shown in Table 1 was done using Minitab 17 Statistical software.

Parameter	Parameter distribution space
External loop radius ( $R_c$ )	48E – 03m to 54E – 03m
Wire radius ( $R_w$ )	46E – 05m to 52E – 05m
Number of loops axially ( $N_a$ )	45 to 51
Number of loops radially ( $N_r$ )	22 to 28

Table 1: Parameter distribution space used in factorial design.

It was done using simulation data based on the complete elliptic integral model given in equation (13). To draw conclusions from the sensitivity analysis, main effects and interaction effects plots were studied. The main effects plot given in Figure 8a describes how the RMSE, defined in equation (2) changes as the value of one parameter is varied. The x-axis on the plot highlights the distribution space through which each parameter is swept across.

How parallel the graph of a parameter is to the x-axis, indicates the degree of variability in the model's output due to the considered distribution space of that parameter. The steeper the slope, the greater the degree of variability due to that input parameter. As seen from the plot, the external radius has the greatest main effect and the wire radius has the least main effect. However, to make a valid conclusion on the most influential parameter, the interaction effects between the parameters need to be analysed. The interaction effects plot is shown in Figure 8b.

In examining the interaction effects plot, lines for two parameters that appear to intersect indicate presence of interaction while lines that appear to be translated and not overlap indicate

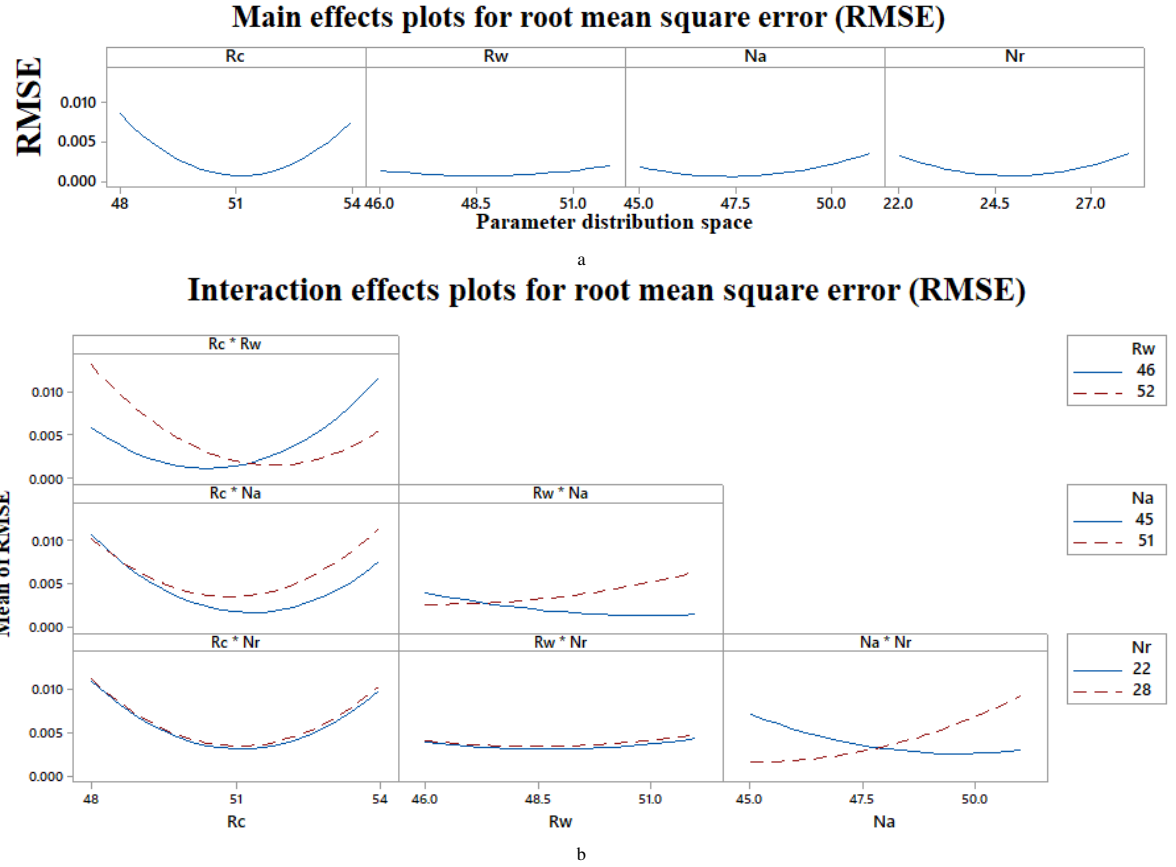


Figure 8: (8a) Main effects plot. How parallel the graph of a parameter is to the  $x$ -axis, indicates the degree of variability in the model's output due to the considered distribution space of that parameter. (8b) Interaction effects plot. Lines for two parameters that appear to intersect indicate presence of interaction while lines that appear to be translated and not overlap indicate no interaction between the parameters.

no interaction between the parameters. It can be observed that, there is no interaction between the external radius and number of loops radially. However, there is a strong interaction between the external radius and wire radius and the number of loops axially and radially. The strong interaction between the external radius and wire radius can be attributed to the fact that the equation used in obtaining the external radius is a function of the wire radius. Hence, only one of them can be used in practice. The model can be simplified by excluding the wire radius because its value can be obtained from measurement data of the manufacturer.

#### 4.3. Numerical solver selection

For parameter identification, several algorithms and optimization methods have been put forth. These algorithms could be categorized into; gradient methods, gradient-free methods and genetic based methods [30]. One algorithm from each of these categories was selected for this case study. Sequential quadratic programming (SQP), Nelder-Mead algorithm and genetic algorithm, all implemented in MATLAB 2019a were considered for calibration. SQP is an effective method used in the optimization of small and large problems having pronounced non-linearities [22]. Nelder-Mead algorithm has been used in parameter estimation where the values of the function are uncertain and subject to noise [31]. Genetic algorithm has been

used to solve optimization problems in which the objective function is discontinuous, stochastic, non-differentiable or nonlinear [32]. To analyse the performance of these algorithms, the metric used was the root mean square error (RMSE).

To select which parameter identification method to use, calibration was first performed using the three different algorithms using simulated data; sequential quadratic programming (SQP) implemented as fmincon in MATLAB, Nelder-Mead algorithm implemented as fminsearch in MATLAB and genetic algorithm. Calibration was done using simulation data on a  $5 \times 5 \times 5$  regular grid.

Simulation data was obtained numerically from the model based on complete elliptic integrals in order to assess the convergence properties of each algorithm. The starting values in implementing the algorithms were the same for all the solvers. Table 2 shows the results of the RMSE percent reduction after calibration using each of the numerical algorithms.

	SQP	Genetic algorithm	Nelder-Mead algorithm
<b>RMSE % reduction</b>	88.4830%	94.1784%	96.4259%

Table 2: Algorithm comparison using simulated data.

It is observed from Table 2 that Nelder-Mead algorithm has the best performance when comparison is done using the percentage reduction of the RMSE. This is followed by genetic algorithm and finally SQP. The performance of SQP could be attributed to using the numerical Jacobian. A lower RMSE indicates that the magnetic field computed by the model closely matches the measured magnetic field. It is desirable that the RMSE is as small as possible. In every calibration done using simulation data, the Nelder-Mead algorithm outperformed the other two. Nelder-Mead algorithm is an unconstrained direct search algorithm. Unlike more traditional optimization methods that use information about the gradient or higher derivatives to search for an optimal point, a direct search algorithm searches a set of points around the current point, looking for one where the value of the objective function is lower than the value at the current point. Direct search methods are used to solve problems for which the objective function is not differentiable, or is discontinuous. The Nelder-Mead method has a commendable performance in the vicinity of the local or global minimum since the intensive computation of the first and second derivative can be avoided [30].

## 5. Calibration results

### 5.1. Simulation of the coil calibration

For simulation purposes the transformation matrix  ${}^wT_{cj}^{(0)}$  in equation (22) was dropped and calibration done only on the parameters to the coil model,  $\xi_m$ . Data used for the simulation was obtained numerically from the model based on complete elliptic integrals proposed in [15] which was shown to be close and accurate enough in computing the magnetic field. Validation was done using simulated data on a  $20 \times 20 \times 20$  regular grid with similar dimensions as the one used for calibration. The ground-truth values, the parameter values before (values used to initialize the numerical algorithm) and after calibration are given in Table 3.

	Ground truth values	Before calibration	After calibration
External loop radius (mm)	51	48	50.069
Wire radius (mm)	0.49	0.46	0.4521
Number of loops axially	48	45	52
Number of loops radially	25	22	23

Table 3: Ground-truth values, parameter values before and after calibration using simulation data.

The following statistical metrics were then studied; maximum error, RMSE and relative error. For a better cross-validation, an additional metric was used, the angular deviation between the measured and modelled fields. The angular deviation is independent from the metrics used for the identification, both by

the data it uses and by its mere definition. Table 4 shows the errors obtained after calibration while Table 5 shows the percent reduction. As expected, the errors after calibration are less than before calibration indicating an improvement in the parameter estimation of the magnetic model.

Absolute error	Before calibration	After calibration
Maximum error(T)	0.0049	0.0033
Root mean square error(T)	$1.1000E - 03$	$4.2622E - 04$

Table 4: Absolute errors before and after calibration using numerical data.

Relative error	Before calibration	After calibration	Percent reduction
Maximum error	0.0097	0.0066	33%
Root mean square error	0.0027	0.0008	64%

Table 5: Reduction of relative errors after calibration using numerical data.

Maximum error is the maximum deviation between the computed magnetic field and the measured magnetic field. A typical location of where the maximum error might be pronounced is on the sides of the coil as opposed to the interested workspace whose dimension is  $100\text{mm}$  by  $100\text{mm}$  by  $50\text{mm}$ . This can be observed in Figure 9.

Table 6 shows the errors obtained in the interested workspace after calibration while Table 7 shows the percent reduction.

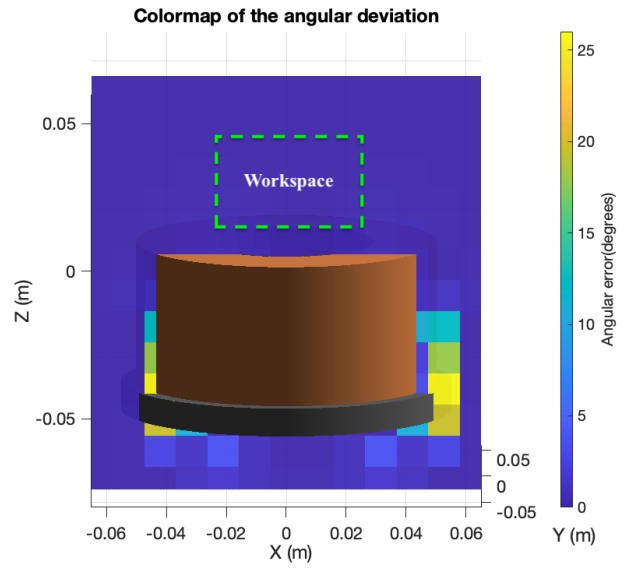
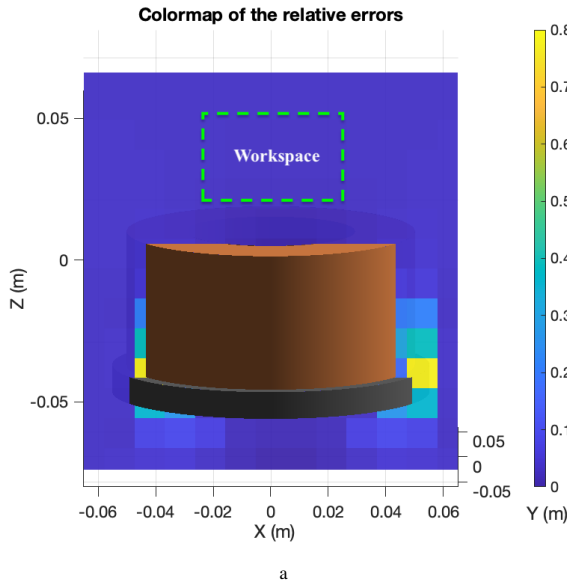
Absolute error	Before calibration	After calibration
Maximum error(T)	$7.7020E - 04$	$4.0204E - 04$
Root mean square error (T)	$4.7405E - 04$	$1.8549E - 04$

Table 6: Absolute errors before and after calibration using numerical data in the interested workspace.

Relative error	Before calibration	After calibration	Percent reduction
Maximum error	0.0027	0.0014	48%
Root mean square error	0.0017	0.0006	65%

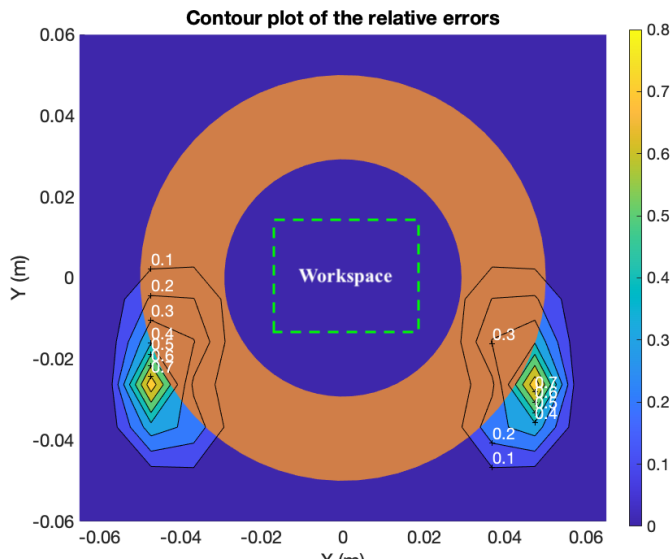
Table 7: Reduction of relative errors after calibration in the interested workspace.

A small RMSE indicates a tight fit of the model to the measurement data. A small as possible RMSE is desired. It is observed that after calibration the RMSE was reduced by 65%. To get a more precise look of where the deviations are, a colourmap of the relative errors and angular deviation in the workspace was plotted. Plots of the relative error in the XZ and the XY plane are as shown in Figure 9a and Figure 9b respectively. Relative

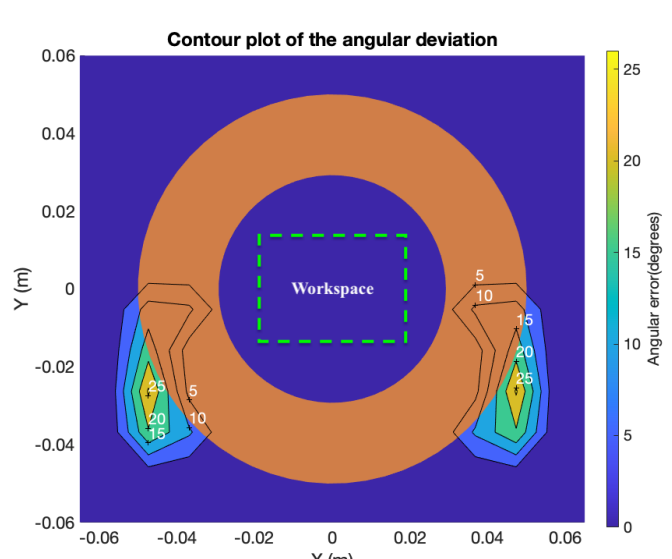


a

a



b



b

Figure 9: Relative errors after calibration using simulated data.

error is the deviation divided by the measured magnetic field at a particular point in the workspace. A higher relative error value indicates a huge deviation at that particular point. From Figure 9a, it is seen that there is a huge magnitude of relative errors on the sides of the coil as opposed to the rest of the workspace. Regardless of the huge errors on the side of the coil, it is not a point of concern since the microrobot during magnetic manipulation will not be placed at that location.

Plots of the angular error in the XZ and the XY plane are as shown in Figure 10a and Figure 10b respectively. The angular deviation illustrates the error between the orientation of the computed field and the measured one. An angular deviation induces an error on both the computed force and torque exerted on the robot during manipulation. It is preferable to have the

angular deviation as low as possible. From the colourmap plot in Figure 10a, a comparison can be drawn to the colourmap plot of relative errors discussed in an earlier paragraph. Majority of the huge magnitude of errors are on the sides of the coil as opposed to the interested workspace. As has been discussed, the huge errors on the side are not a point of concern during magnetic manipulation since the robot will not be placed at that particular location.

## 5.2. Experiment

For the physical experiment, magnetic field measurement data was collected in a  $5 \times 5 \times 5$  as well as in a  $8 \times 8 \times 8$  equally spaced grid. To generate the measurement grid, the coil was translated in its X, Y, Z direction with the help of a serial robot

(Universal robot 3) arm while the sensor was held in a fixed position on the worktable as shown in Figure 11. The former grid was used for calibration while the latter for validation. The data was collected in a workspace of length, 100mm, width 100mm and height, 50mm. This workspace is close to the coil and is the area of interest in magnetic manipulation.

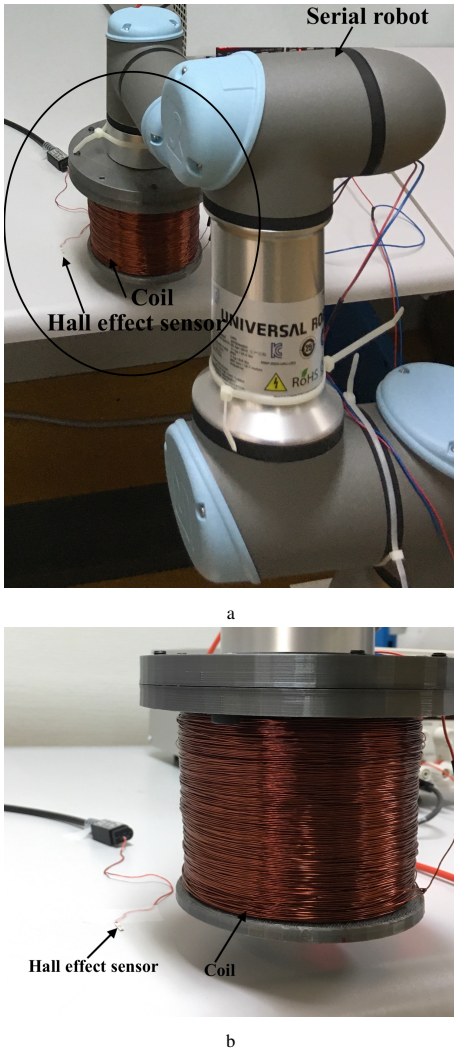


Figure 11: (11a) Experimental setup showing the serial robot, coil and Hall effect sensor. (11b) Zoom on the Hall effect sensor and coil.

Measurement data was collected using a Hall effect sensor, THM1176 from Metrolab. It is a 3-axis Hall magnetometer that has a range from  $100\mu T$  to  $14T$ . The sensor also simultaneously measured the magnetic field in all the three axes ( $X, Y, Z$ ). Current was provided to the coil through a power supply and to ascertain that the right current magnitude was being delivered to the coil, a multimeter was connected in the circuit. EZMag3D software from Metrolab was then used in data acquisition of the magnetic field from the sensor.

Parameter identification using equation (22) was done in MATLAB using the Nelder-Mead algorithm. Parameters of the magnetic coil,  $\xi_m$  and the transformation matrix  ${}^wT_{c_j}^{(0)}$  obtained from physical measurements used to initialize the algorithm and the values after calibration are given in Table 8.

	Parameter values from physical measurements	Parameter values after calibration
External loop radius(mm)	46.5	53.32
Wire radius(mm)	0.30	0.346
Number of loops axially	115	110
Number of loops radially	54	46
Translation in the X-axis (mm)	-42.0	-31.78
Translation in the Y-axis (mm)	-26.0	-36.20
Translation in the Z-axis (mm)	17.0	22.00
Rotation in the X-axis (rad)	1.57	1.748
Rotation in the Y-axis (rad)	0	0
Rotation in the Z-axis (rad)	0	0

Table 8: Parameter values before and after calibration.

Similarly to the simulation results, Table 9 shows the errors obtained after calibration while Table 10 shows the percent reduction. On performing validation, it was observed that the RMSE between the model and measurements was reduced by 37% after calibration.

Absolute error	Before calibration	After calibration
Maximum error(T)	0.0092	0.0074
Root mean square error(T)	0.0043	0.0027

Table 9: Absolute errors before and after calibration using experimental data.

Relative error	Before calibration	After calibration	Percent reduction
Maximum error	0.0885	0.0674	23%
Root mean square error	0.0414	0.0260	37%

Table 10: Reduction of relative errors after calibration using experimental data.

Plot of the relative error and the angular deviation in the interested workspace are as shown in Figure 12 and Figure 13 respectively. The magnitude of errors obtained using experimental data was observed to be much greater than those obtained using simulation data. This may be attributed to the positioning accuracy of the serial robot and numerical errors that may have arisen during processing of the collected data.

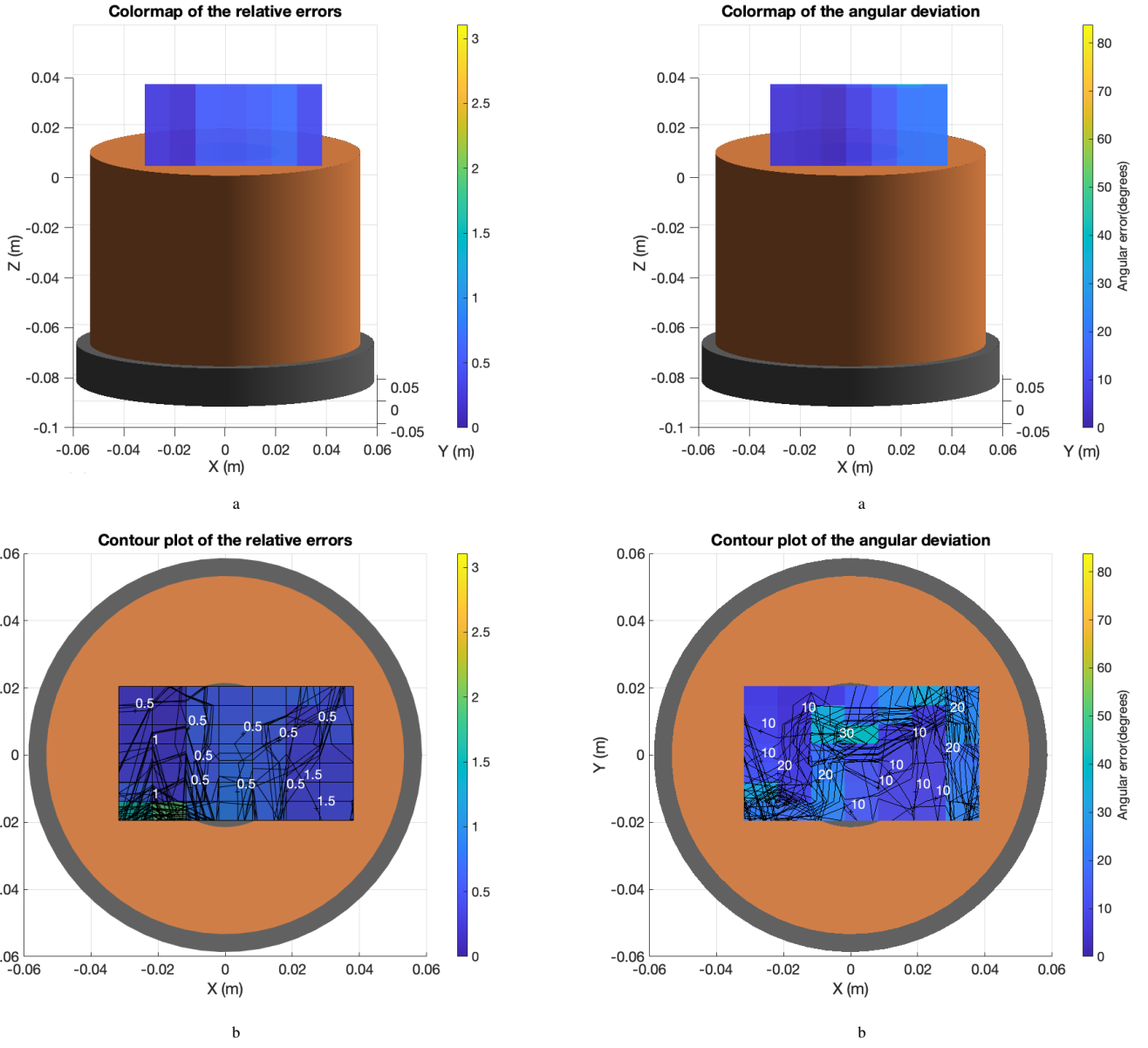


Figure 12: Relative errors after calibration using experimental data.

## 6. Conclusions and perspectives

A calibration protocol used to calibrate a magnetic manipulation system with multiple mobile coils has been presented. The magnetic manipulation system was subdivided and each coil calibrated separately assuming the superposition theorem holds and that the robotic arms are perfectly calibrated. A control-oriented magnetic model based on complete elliptic integrals with its continuity extension was used. The protocol involved identifying model parameter values to the electromagnetic system by use of the Nelder-Mead algorithm. Calibration was performed on both numerically generated data, as well as data measured from a physical system. It was observed that the root mean square error was reduced after calibration indicating an increase on the model accuracy. A minimum as possible value of the root mean square error is desired. In this research, it

was assumed that the kinematic parameters to the serial robot were perfectly known. In a case where they are not known, the serial robot needs to be decoupled from the coil and its calibration done separately. It was also assumed that the superposition theorem holds and that there are no couplings between the electromagnets. This assumption might not always be true especially when the coils are too close to each other and could open up further research paths related to electromagnetics. In future works, advanced control strategies to magnetically navigate surgical instruments in relevant medical procedures will be developed. The capabilities of our magnetic manipulation system will also be improved by introducing ferromagnetic-cores in the coils so as to achieve stronger magnetic fields. The introduction of such cores would necessitate modification of our control-oriented model.

## 7. Acknowledgements

This work is part of Multiflag project (ANR-16-CE33-0019) funded by the French National Research Agency (ANR). It was also supported by EIPHI Graduate School (Contract No. ANR-17-EURE-0002), by Région Bourgogne Franche-Comté through the COErCIVe project and by the Grand Prix Scientifique 2018, Fondation Charles Defforey, Institut de France.

## References

- [1] M. Kim, A. A. Julius, U. K. Cheang (Eds.), *Microbiorobotics: biologically inspired microscale robotic systems*, Micro & nano technologies series, Elsevier, Amsterdam, 2017.
- [2] J. Sikorski, C. M. Heunis, F. Franco, S. Misra, The ARMM System: An Optimized Mobile Electromagnetic Coil for Non-Linear Actuation of Flexible Surgical Instruments, *IEEE Transactions on Magnetics* 55 (9) (2019) 1–9. doi:10.1109/TMAG.2019.2917370.
- [3] J. J. Abbott, E. Diller, A. J. Petruska, Magnetic Methods in Robotics, *Annual Review of Control, Robotics, and Autonomous Systems* 3 (1) (2020) 57–90. doi:10.1146/annurev-control-081219-082713.
- [4] B. J. Nelson, I. K. Kaliakatsos, J. J. Abbott, Microrobots for minimally invasive medicine, *Annual review of biomedical engineering* 12 (2010) 55–85, publisher: Annual Reviews.
- [5] M. J. Mack, Minimally Invasive and Robotic Surgery, *JAMA* 285 (5) (2001) 568. doi:10.1001/jama.285.5.568.
- [6] J. Sikorski, A. Denasi, G. Bucchi, S. Scheggi, S. Misra, Vision-Based 3-D Control of Magnetically Actuated Catheter Using BigMag—An Array of Mobile Electromagnetic Coils, *IEEE/ASME Transactions on Mechatronics* 24 (2) (2019) 505–516. doi:10.1109/TMECH.2019.2893166.
- [7] L. Yang, X. Du, E. Yu, D. Jin, L. Zhang, DeltaMag: An Electromagnetic Manipulation System with Parallel Mobile Coils, in: 2019 International Conference on Robotics and Automation (ICRA), IEEE, Montreal, QC, Canada, 2019, pp. 9814–9820. doi:10.1109/ICRA.2019.8793543.
- [8] B. Veron, A. Hubert, J. Abadie, N. Andreff, Dealing with redundancy of a multiple mobile coil magnetic manipulator: A 3rpr magnetic parallel kinematics manipulator, in: ARK, 2016, pp. 201–208.
- [9] J. Sikorski, I. Dawson, A. Denasi, E. E. Hekman, S. Misra, Introducing BigMag — A novel system for 3D magnetic actuation of flexible surgical manipulators, in: 2017 IEEE International Conference on Robotics and Automation (ICRA), IEEE, Singapore, Singapore, 2017, pp. 3594–3599. doi:10.1109/ICRA.2017.7989413.
- [10] R. Chen, D. Folio, A. Ferreira, Study of robotized electromagnetic actuation system for magnetic microrobots devoted to minimally invasive ophthalmic surgery, in: 2019 International Symposium on Medical Robotics (ISMR), IEEE, 2019, pp. 1–7. doi:10.1109/ISMR.2019.8710208.
- [11] R. Chen, D. Folio, A. Ferreira, Mathematical approach for the design configuration of magnetic system with multiple electromagnets, *Robotics and Autonomous Systems* 135 (2021) 103674.
- [12] C. Chautems, B. J. Nelson, The tethered magnet: Force and 5-DOF pose control for cardiac ablation, in: 2017 IEEE International Conference on Robotics and Automation (ICRA), IEEE, 2017, pp. 4837–4842. doi:10.1109/ICRA.2017.7989562.
- [13] S. Chowdhury, W. Jing, D. J. Cappelleri, Controlling multiple micro-robots: recent progress and future challenges, *Journal of Micro-Bio Robotics* 10 (1-4) (2015) 1–11. doi:10.1007/s12213-015-0083-6.
- [14] A. J. Petruska, J. J. Abbott, Optimal permanent-magnet geometries for dipole field approximation, *IEEE Transactions on Magnetics* 49 (2) (2013) 811–819. doi:10.1109/TMAG.2012.2205014.
- [15] M. Etievant, A. Bolopion, S. Regnier, N. Andreff, An Improved Control-Oriented Modeling of the Magnetic Field, in: 2019 International Conference on Robotics and Automation (ICRA), IEEE, Montreal, QC, Canada, 2019, pp. 6178–6184. doi:10.1109/ICRA.2019.8793679.
- [16] R. Bernhardt, S. L. Albright (Eds.), *Robot calibration*, 1st Edition, Chapman & Hall, London ; New York, 1993.
- [17] R. Johansson, *System Modeling and Identification*, Information and system sciences series, Prentice Hall, 1993.
- [18] A. Elatta, F. L. Zhi, Y. Daoyuan, L. Fei, L. Pei Gen, An Overview of Robot Calibration, *Information Technology Journal* 3 (1) (2004) 74–78. doi:10.3923/itj.2004.74.78.
- [19] A. J. Petruska, J. Edelmann, B. J. Nelson, Model-Based Calibration for Magnetic Manipulation, *IEEE Transactions on Magnetics* 53 (7) (2017) 1–6. doi:10.1109/TMAG.2017.2653080.
- [20] L. Ljung, *System identification: theory for the user*, 2nd Edition, Prentice Hall information and system sciences series, Prentice Hall PTR, 1999.
- [21] T. Söderström, P. Stoica, *System Identification*, Prentice-Hall, Inc., USA, 1988.
- [22] J. Nocedal, Wright ,Stephen J, *Numerical Optimization*, Springer Series in Operations Research and Financial Engineering, Springer New York, 2006. doi:10.1007/978-0-387-40065-5.
- [23] R. Schill, General relation for the vector magnetic field of a circular current loop: a closer look, *IEEE Transactions on Magnetics* 39 (2) (2003) 961–967. doi:10.1109/TMAG.2003.808597.
- [24] I. S. Grant, W. R. Phillips, *Electromagnetism*, 2nd Edition, The Manchester physics series, Wiley, Chichester [England] ; New York, 1990.
- [25] P. Renaud, N. Andreff, J.-M. Lavest, M. Dhome, Simplifying the kinematic calibration of parallel mechanisms using vision-based metrology, *IEEE Transactions on Robotics* 22 (1) (2006) 12–22. doi:10.1109/TRO.2005.861482.
- [26] R. Horraud, F. Dornaika, Hand-eye calibration, *The International Journal of Robotics Research* 14 (3) (1995) 195–210. doi:10.1177/027836499501400301.
- [27] N. Andreff, R. Horraud, B. Espiau, Robot hand-eye calibration using structure-from-motion, *The International Journal of Robotics Research* 20 (3) (2001) 228–248. doi:10.1177/02783640122067372.
- [28] S. Ray, J. Mukherjee, S. Mandal, Modelling nitrogen and carbon cycles in Hooghly estuary along with adjacent mangrove ecosystem, in: *Developments in Environmental Modelling*, Vol. 27, Elsevier, 2015, pp. 289–320. doi:10.1016/B978-0-444-63536-5.00013-2.
- [29] J. Ochoa Robles, S. De-León Almaraz, C. Azzaro-Pantel, Design of experiments for sensitivity analysis of a hydrogen supply chain design model, *Process Integration and Optimization for Sustainability* 2 (2) (2018) 95–116. doi:10.1007/s41660-017-0025-y.
- [30] Betsaida Lo-Amni Fernández Difo, *Automated Calibration for Numerical Models of Riverflow*, Ph.D. thesis, University of Stuttgart - Institute for Modelling Hydraulic and Environmental Systems (Nov. 2016).
- [31] J. Larson, M. Menickelly, S. M. Wild, Derivative-free optimization methods, *Acta Numerica* 28 (2019) 287–404. doi:10.1017/S0962492919000060.
- [32] F. Tao, L. Zhang, Y. Laili, *Configurable Intelligent Optimization Algorithm*, Springer Series in Advanced Manufacturing, Springer International Publishing, Cham, 2015. doi:10.1007/978-3-319-08840-2.